

# Catalysis Science & Technology

Accepted Manuscript



This is an *Accepted Manuscript*, which has been through the Royal Society of Chemistry peer review process and has been accepted for publication.

*Accepted Manuscripts* are published online shortly after acceptance, before technical editing, formatting and proof reading. Using this free service, authors can make their results available to the community, in citable form, before we publish the edited article. We will replace this *Accepted Manuscript* with the edited and formatted *Advance Article* as soon as it is available.

You can find more information about *Accepted Manuscripts* in the [Information for Authors](#).

Please note that technical editing may introduce minor changes to the text and/or graphics, which may alter content. The journal's standard [Terms & Conditions](#) and the [Ethical guidelines](#) still apply. In no event shall the Royal Society of Chemistry be held responsible for any errors or omissions in this *Accepted Manuscript* or any consequences arising from the use of any information it contains.

Cite this: DOI: 10.1039/c0xx00000x

[www.rsc.org/xxxxxx](http://www.rsc.org/xxxxxx)

ARTICLE TYPE

# Surface stabilities and NO oxidation kinetics on hexagonal-phase LaCoO<sub>3</sub> facets: a first-principles study

Xiao Liu,<sup>a,b</sup> Zhengzheng Chen,<sup>b</sup> Yanwei Wen,<sup>b</sup> Rong Chen<sup>\*a</sup> and Bin Shan<sup>\*b,c</sup>

Received (in XXX, XXX) Xth XXXXXXXXX 20XX, Accepted Xth XXXXXXXXX 20XX

DOI: 10.1039/b000000x

LaCoO<sub>3</sub> perovskite has recently received great attention as a potential alternative to precious metal based NO oxidation catalyst. We report here a comprehensive first-principles study of the NO oxidation kinetics on differently re-constructed hexagonal-phase LaCoO<sub>3</sub> facets. Among the 42 low-index facets considered, (1  $\bar{1}$  02) LaO-, ( $\bar{1}$  104) O<sub>2</sub>- and (0001) LaO<sub>3</sub>- terminated facets are found to be thermodynamically stable and likely to be exposed in LaCoO<sub>3</sub> oxide nanoparticles. Among these stable facets, (0001) LaO<sub>3</sub>-terminated surface is catalytically most active towards NO oxidation, with the reaction proceeding through the mono-vacancy Mars-van Krevelen mechanism. Our study shed light on the atomistic scale NO oxidation mechanism on LaCoO<sub>3</sub> facets and can help further optimization of the catalyst.

## 1. Introduction

Diesel engines have aroused great interests in recent years due to their high fuel efficiencies and low green-house gas emissions.<sup>1</sup> However, the lean burn exhaust which contains considerable amount of nitrogen oxides (NO<sub>x</sub>) poses great threat to human health and environment. Two mainstream technologies are being utilized by auto manufacturers to remove the hazardous NO<sub>x</sub> emissions. The first strategy is called selective catalytic reduction (SCR), which involves the partial oxidation of NO to NO<sub>2</sub> through diesel engine oxidation (DOC) catalysts and subsequent reactions with ammonia to form environmentally benign N<sub>2</sub>. The other popular strategy is lean NO<sub>x</sub> trap (LNT), which utilizes the NO<sub>2</sub> storage and release mechanism of LNT trapping materials such as Pt/BaO/Al<sub>2</sub>O<sub>3</sub> for NO<sub>x</sub> reduction. In both cases, a higher concentration of NO<sub>2</sub> in the exhaust stream proves to be beneficial for the catalytic process,<sup>2</sup> driving a considerable interest in the scientific community in search of catalysts for efficiently oxidizing NO into NO<sub>2</sub>. Traditionally, platinum (Pt) metal is the major material component in automobile catalytic converters for NO oxidation due to its durability against oxidation and high catalytic activity originating from the unique *d*-orbital electronic structure.<sup>3,4</sup> However, with the urge of stricter NO<sub>x</sub> control in the next-generation emission standards, its practical development and large-scale applications are hindered by limited reserves and supply. Pt's rising price and the higher catalyst loading for the stricter emission standards also likely raise cost concerns for auto manufacturers. To reduce the overall catalyst cost, precious metal catalysts need to be replaced by new earth-abundant, cost effective, and high performance catalysts.

Significant amount of work has been undertaken in the field of

emission control technology to search for alternative NO oxidation catalysts. Rare-earth and transition metal oxide catalysts have long been considered as one of the most promising candidates for substituting expensive precious metals components, as it shows not only thermal stability towards sintering and oxidation, but also excellent catalytic activity for many important chemical reactions, such as CO oxidation, hydrocarbon oxidation, NO oxidation, NO<sub>x</sub> storage and reduction.<sup>5-10</sup> Hua et al.<sup>11</sup> have synthesized Mn-Ce-O<sub>x</sub> catalysts at various ratios via co-precipitation, low temperature solid phase reaction and citric acid methods and studied the activity for NO oxidation. While MnO<sub>x</sub> has shown promising catalytic activity, it suffers from aging loss of catalytic activity during an extended period of catalytic reactions. More recently, Wang et al. have reported mullite based oxide catalyst where Mn-Mn dimer serves as the catalytic reaction center for NO oxidation.<sup>12</sup> Among different types of oxides investigated thus far, perovskite structures (ABO<sub>3</sub>, with A = rare-earth cation and B = transition metal cation), particular LaCoO<sub>3</sub>, have attracted much attention as Pt replacement catalyst. Wen et al. and Zhou et al. have studied the NO oxidation activity of cerium (Ce) and copper (Cu) doped LaCoO<sub>3</sub> perovskite and showed that A and B site substitution can greatly enhance the performance.<sup>13,14</sup> Kim et al.<sup>15</sup> found that strontium (Sr) doped LaCoO<sub>3</sub> has great performance for NO oxidation which is comparable with commercial Pt/ $\gamma$ -Al<sub>2</sub>O<sub>3</sub> based catalyst. On the theoretical side, efforts in understanding the electronic structures of LaCoO<sub>3</sub> materials as well as its surface stabilities are also emerging. Kahn et al. have studied the stability of cubic LaCoO<sub>3</sub> using Born shell empirical model and predicted the Co-terminated (111) surface and LaCoO-terminated (110) surface to be most stable.<sup>16</sup> To take into account the charge redistribution in a self-consistent manner and improve the accuracy of stable facets prediction, Chen et al. have used ab initio thermodynamics models to construct the crystal morphology of cubic LaCoO<sub>3</sub>

nanoparticles and found that LaO-terminated (001) surface is more stable on the other hand.<sup>17</sup> However, both stability studies focused mostly on the structural and electronic properties of cubic phase LaCoO<sub>3</sub> which is in not in agreement with the experimental characterizations of the LaCoO<sub>3</sub> ground state. A number of studies have revealed that hexagonal phase LaCoO<sub>3</sub> is lower in energy than cubic phase,<sup>18,19</sup> in good agreement with the XRD identification of the R $\bar{3}c$  space group of the LaCoO<sub>3</sub>.<sup>20,21</sup> Recently, Choi et al. have studied the NO oxidation reaction on cubic-phase LaCoO<sub>3</sub> with Jahn-Teller (J-T) distortion and discussed the role of Sr in enhancing the oxygen exchange ability on one particular facet.<sup>22</sup> To our best knowledge, a detailed and comprehensive knowledge of NO oxidation kinetics on different LaCoO<sub>3</sub> perovskite facets is still lacking. To further optimize the nanoparticle catalyst for industrial use, it is of great importance to gain a deep understanding of underlying active sites and reaction mechanisms at the atomic level.

In this study, we report comprehensive first-principles calculations on the surface stabilities of differently re-constructed hexagonal-phase LaCoO<sub>3</sub> oxide catalyst and the NO oxidation kinetics on stable facets. By comparing surface grand potentials, we identified the stable facets of LaCoO<sub>3</sub> in different chemical environments. Wulff-construction was used as a first-order approximation to predict the exposed facets in LaCoO<sub>3</sub> nanoparticles. NO oxidation energetics and kinetics on these catalytically active facets were investigated in detail. Our results show that LaO<sub>3</sub>-terminated surface is the catalytically most active surface for NO oxidation, whose surface area depends sensitively on the cobalt chemical potential. The rest of the paper is organized as follows: In Sec. II, we briefly summarize the model system and computational methodology. Detailed results and discussions are presented in Sec. III. Finally, summary and conclusions are given in Sec. IV

## 2. Computational models and methods

For comparison purposes, the atomic structures of cubic phase LaCoO<sub>3</sub> was shown in Figure 1(a), with La atoms (green spheres) in eight corners, one Co atom (blue sphere) at the center of the unit cell, and O atoms (red spheres) located at the center of facets. Figure 1(b) shows the cross section of cubic (100)-CoO<sub>2</sub> surface. A distinctive feature of the cubic phase is the Co-O-Co bond angle of 180°. The hexagonal phase LaCoO<sub>3</sub> also consists of CoO<sub>6</sub> octahedral and La atoms in the vertex as shown by the red dotted lines in Figure 1(c). However, the structure and symmetry are different from the cubic phase due to the J-T distortion, which causes the distortions in the red dotted framework, making it no longer the unit cell of the structure.<sup>23,24</sup> Figure 1(d) shows the (1 $\bar{1}$ 02)-CoO<sub>2</sub> surface in hexagonal phase, which roughly corresponds to the (100)-CoO<sub>2</sub> surface in cubic phase. Note that the Co-O-Co bond angle in hexagonal phase is 161.9° instead of 180°. J-T distortion also makes certain symmetric directions in the cubic phase inequivalent. For example, the eight equivalent <111> directions in cubic phase now split to two <0001> and six < $\bar{1}$ 101> directions in the hexagonal phase. The twelve <110> directions in cubic phase now become six <11 $\bar{2}$ 0> and six < $\bar{1}$ 104> directions in the hexagonal phase (the detailed correspondence relationships can be found in Supplementary Information (SI)). In the surface stability discussion part, we

have considered all these non-equivalent directions.

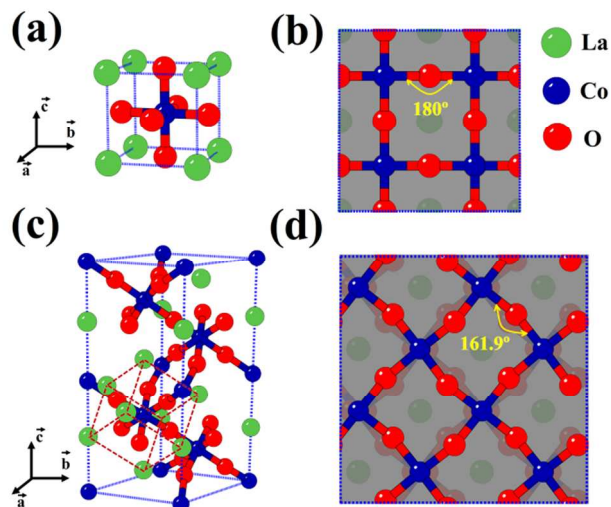


**Fig.1** Atomic structures of (a) cubic phase and (c) hexagonal phase LaCoO<sub>3</sub>. The similar cubic structure has been labeled by red dotted lines, which is not the unit cell of hexagonal phase. Top view of (b) (100)-CoO<sub>2</sub> surface in cubic phase and (d) (1 $\bar{1}$ 02)-CoO<sub>2</sub> surface in hexagonal phase have been presented.

All calculations were performed within the density functional theory (DFT)<sup>25,26</sup> framework using plane wave basis as implemented in Vienna ab initio simulation package (VASP)<sup>27-29</sup>. The exchange and correlation energy was treated by generalized gradient approximation (GGA) with Perdew-Burke-Ernzerhof (PBE)<sup>30</sup> form generated by the projector augmented wave (PAW)<sup>31</sup> method, as such functional was shown to give reasonable results for molecular adsorption energies.<sup>32,33</sup> For Co ions, the outer electrons ( $3d^84s^1$ ) were treated as valence electrons and the core electrons were replaced by effective potentials. While standard DFT methods have been successfully used to investigate electronic structures and catalytic properties of metal and metal oxides surfaces, it fails to obtain the correct electronic structure for strongly correlated systems such as transition metal oxides and rare-earth compounds. To overcome the inaccuracy of standard DFT in describing the partially filled *d*-states in Co<sup>3+</sup> ions, we used GGA + *U* formalism to correct the on-site Coulomb and exchange interactions for localized *d* orbitals.<sup>34</sup> Several methods have been proposed to determine the magnitude of the onsite Hubbard-type *U* and detailed procedures in getting *U* values have been discussed extensively in the review paper by Lee et al.<sup>23</sup> In general, the inclusion of *U* correction is shown to yield much better results in terms of describing electronic structures and can recover most of the bulk and surface properties, as illustrated in the case of predicting CO/NiO and NO/NiO adsorption energies.<sup>35,36</sup> Recently, Ma et al. performed a systematic comparative study on the influence of *U*, *J* parameters in describing LaCoO<sub>3</sub> perovskite properties and found a set of optimal values of *U*=3.40 eV and *J*=0.49 eV that offer results in good agreement with experiments.<sup>37</sup> We adopted the aforementioned *U*, *J* parameters in the present work. Recent progresses in GW calculations<sup>38,39</sup> or hybrid functional calculations<sup>40,41</sup> can in principle yield reliable results with less empirical parameters. However, due to the high computational

demand of these methods and the practical need of using a large unit cell for modeling surface reactions, we chose GGA +  $U$  formalism as a good compromise between accuracy and computational efficiency.

In both bulk and surface calculations, the geometry optimization is performed till the Hellmann-Feynman force on each atom is smaller than 0.05 eV/Å. An energy cutoff of 400 eV is employed on the plane wave basis. The numerical integration in the first Brillouin zone is performed using a Monkhorst-Pack<sup>42</sup> grid of  $7 \times 7 \times 3$  for the bulk, and  $3 \times 3 \times 1$  for the surface, respectively. To check the convergence, we have compared the total energy to the ones calculated with finer  $k$ -mesh. The difference is smaller than 5 meV. The LaCoO<sub>3</sub> surfaces were represented by periodic slabs consisting of at least 11 layers. A vacuum with thickness of 15 Å is adopted to avoid the interaction between images slabs. In order to discuss the surfaces' thermodynamic stability, we have calculated the surface grand potential ( $\Omega$ ), which has been previously used in studies of low-index surfaces of binary and ternary compounds.<sup>43,44</sup> By assuming that the slab is always in equilibrium with the bulk LaCoO<sub>3</sub>, we have the following constraint:

$$E_{LaCoO_3} = \mu_{LaCoO_3} = \mu_{La} + \mu_{Co} + 3\mu_O \quad (1)$$

where  $E_{LaCoO_3}$  is the total energy of bulk per formula unit LaCoO<sub>3</sub>,  $\mu_i$  is the chemical potential of the  $i$ -th species. By substituting  $\mu_{La}$ ,  $\Omega$  can be expressed as a function of  $\mu_O$  and  $\mu_{Co}$ :

$$\Omega = \frac{1}{2S} [E_{slab} - N_{La}E_{LaCoO_3} - \mu_O(N_O - 3N_{La}) - \mu_{Co}(N_{Co} - N_{La})] \quad (2)$$

where  $E_{slab}$  is the energy of slab.  $N_{La}$ ,  $N_{Co}$  and  $N_O$  are the number of atoms in the slab,  $S$  is the surface area of the slab and the factor of 1/2 comes from the fact that the slab has identical top and bottom terminations. Boundary conditions have also been considered to define the accessible region of the thermodynamic system. To avoid condensation of elemental La, Co or O<sub>2</sub>(g) on surfaces, the following three constraints have to be satisfied:

$$\mu_{Co} + 3\mu_O \geq E_{LaCoO_3} - \mu_{La} \quad (3)$$

$$\mu_{Co} \leq \mu_{Co}^0 \quad (4)$$

$$\mu_O \leq \mu_O^0 \quad (5)$$

where  $\mu_{La}^0$  ( $\mu_{Co}^0$ ) is the cohesive energy of La (Co) bulk atom, and  $\mu_O^0$  is  $E_{O_2}/2$ , where  $E_{O_2}$  is the energy of an O<sub>2</sub> molecule. Detailed derivation of the boundary conditions can be found in Ref. 43.

After obtaining  $\Omega$  for all ideal and re-constructed surfaces, we employed Wulff-construction<sup>45</sup> as a first-order approximation to predict the exposed facets of LaCoO<sub>3</sub> perovskite nanoparticles. The distances between the parallel exposed facets are proportional to  $\Omega$ , which determines the shape of nanoparticles. The followed nanoparticles are all generated using the Visualization for Electronic and Structural Analysis (VESTA) software.<sup>46</sup> Two quantities are of great importance to the activity of exposed oxide surfaces: oxygen vacancy energy ( $E_{Ov}$ ) and the highest energy barrier ( $\Delta E_{TS}$ ) in the minimum energy path (MEP) of the NO oxidation process. In current work,  $E_{Ov}$  is calculated using the following formula:

$$E_{Ov} = E_{sys-O} - E_{sys} + E_{O_2}/2 \quad (6)$$

where,  $E_{sys}$  and  $E_{sys-O}$  are the total energies of ideal and defective (with one oxygen vacancy) hexagonal LaCoO<sub>3</sub> slabs, respectively. For the MEP of NO oxidation, the climbing image nudged elastic band method (CI-NEB)<sup>47</sup> was employed. Initial approximations to reaction paths are obtained by linear interpolation between the reactant and product configurations. Six intermediate images were used for all CI-NEB calculations, which map the MEP with reasonable accuracy. Moreover, frequency calculation has been performed to check the transition states and only one imaginary frequency exists for each transition state.

## 3. Results and discussion

### 3.1. Bulk properties

The calculated bulk properties of LaCoO<sub>3</sub> in hexagonal phase such as the lattice constants ( $a$  and  $c$ ), band gap ( $E_g$ ), magnetic moment ( $\mu$ ) and total energy ( $E_{LaCoO_3}$ ) of LaCoO<sub>3</sub> are tabulated in Table 1. During the optimization of lattice constants, we keep  $\alpha=\beta=90^\circ$ ,  $\gamma=120^\circ$  and  $a=b$ . The values of  $a$  and  $c$  are optimized to get the minimal total energy. Experimental values are also listed for comparison. The results show that the hexagonal phase of LaCoO<sub>3</sub> is indeed the ground state since the total energy per unit is about 0.2~0.3 eV lower than that of the cubic phase. Note that the non-spin-polarized model (NSP) with PBE+ $U$  yields almost identical results with spin-polarized model (SP) and it recovers the experimental lattice constant within 0.3%<sup>48</sup>, and the band gap within 0.01 eV<sup>49</sup>. Previous theoretical and experimental studies also indicate LaCoO<sub>3</sub> is a nonmagnetic semiconductor with Co<sup>3+</sup> in the low-spin state ( $S=0$ ,  $t_{2g}^6 e_g^0$ ).<sup>50-52</sup> Overall, the NSP model is computationally efficient and yields reliable results about the structural and electronic properties of LaCoO<sub>3</sub>. It is thus employed in all the following calculations. For gas molecules such as O<sub>2</sub>, NO and NO<sub>2</sub>, their total energies have been corrected by spin polarizations using the same techniques as reported in previous studies.<sup>53-55</sup>

**Table 1.** Lattice constant  $a$  ( $a = b$ ) and  $c$ , band gap  $E_g$ , magnetic moment  $\mu$  and total energy  $E_{LaCoO_3}$  per unit of LaCoO<sub>3</sub>. Values in the parenthesis in the last column are in cubic phase. For PBE and PBE+ $U$  ( $U = 3.40$  eV), we have considered both spin-polarized (SP) and non-spin-polarized (NSP) models. For comparison, available experimental data are listed in the bottom row as well.

	$a$ (Å)	$c$ (Å)	$E_g$ (eV)	$\mu$ ( $\mu_B$ )	$E_{LaCoO_3}$ (eV)
SP	5.426	12.991	0.00	0.02	-38.00 (-37.72)
NSP	5.427	12.949	0.00	-	-37.99 (-37.74)
SP- $U$	5.426	12.991	0.63	0.00	-36.15 (-35.90)
NSP- $U$	5.424	12.960	0.61	-	-36.14 (-35.90)
Exp.	5.426 <sup>a</sup>	12.991 <sup>a</sup>	0.60 <sup>b</sup>	0.00	-

<sup>a</sup>Ref. 48 and <sup>b</sup>Ref. 49.

The calculated band structure and density of states (DOS) are shown in Figure 2. The sharp anti-bonding peak represents the vacant La 4*f* orbitals at around 4.5 eV above the Fermi level. The occupied 3*d* orbitals of Co were split into  $t_{2g}$  (-5 ~ 3.5 eV) and  $e_g$

(-1 ~ 0 eV) via the cubic symmetry breaking process. It is found the Co-3d and O-2p orbitals contribute most to the valence band maximum and the conduction band minimum. Figure 2 also shows strong hybridization between Co-3d and O-2p orbitals, indicating the stability of CoO<sub>6</sub> octahedrons in LaCoO<sub>3</sub>.

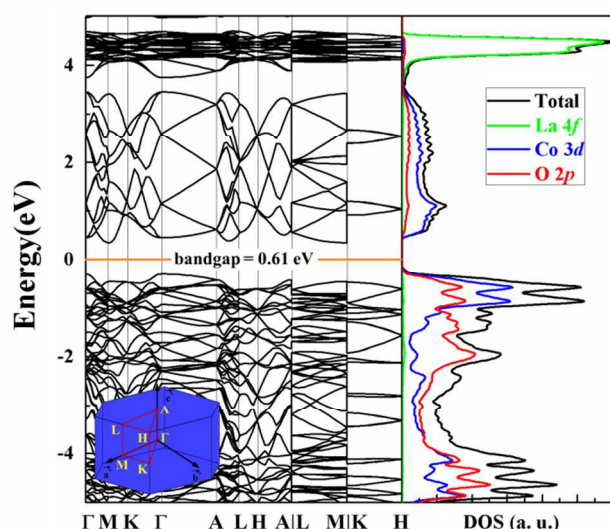


**Fig.2** The band structure and DOS of LaCoO<sub>3</sub>. The total density of states (DOS) and partial DOS (PDOS) of La 4f, Co 3d and O 2p orbitals are plotted with black, green, blue and red lines, respectively.

### 3.2. Surface stability

According to the symmetry of hexagonal phase LaCoO<sub>3</sub>, we have considered six low-index crystalline plane families: {1102}, {0001} and {1101}, {1120} and {1104}, {1010}. Each family has two different terminations. We label them in the format that (orientation)-terminated elements, such as (1102)-LaO and -CoO<sub>2</sub>, (0001)-LaO<sub>3</sub> and -Co, (1101)-LaO<sub>3</sub> and -Co, (1120)-LaCoO and -O<sub>2</sub>, (1104)-LaCoO and -O<sub>2</sub>, (1010)-LaCoO and -O<sub>2</sub> facets, and present their detailed structures in Figure S2-S5 in SI. Since these facets have the nominal charges of La (+3e) Co (+3e) and O (-2e) atoms, they are polarized and may undergo reconstruction.<sup>56</sup>

We used  $p(1\times 1)$  to represent an ideal surface,  $p(2\times 1)$  and  $p(2\times 2)$  to represent two different kinds of reconstructions. Moreover, for O<sub>2</sub> terminated surfaces: (1010)-O<sub>2</sub>, (1120)-O<sub>2</sub> and (1104)-O<sub>2</sub>,  $c(2\times 1)$  and  $c(2\times 2)$  reconstruction were also considered.<sup>57</sup> All 25 reconstruction rules considered are presented in Figure S6 in SI.

The surface grand potentials ( $\Omega_s$ ) of a total of 42 facets have been calculated. The grand surface energy at  $\Delta\mu_{\text{Co}} = \Delta\mu_{\text{O}} = 0$  eV ( $\Omega_0$ ) and the stoichiometric ratio of the slabs, where  $\Delta\mu_{\text{Co}} = \mu_{\text{Co}} - \mu_{\text{Co}}^0$  and  $\Delta\mu_{\text{O}} = \mu_{\text{O}} - \mu_{\text{O}}^0$  are summarized in Table S1 in SI. By choosing the surface with the lowest  $\Omega$  at each point in accessible region (defined by confinements Eqs. (3)-(5)), the surface stability diagram of hexagonal phase LaCoO<sub>3</sub> can be constructed as shown in Figure 3(a). We find that three terminations out of 42 facets are thermodynamically most favorable: (1104)-O<sub>2</sub>  $c(2\times 2)$ , (0001)-LaO<sub>3</sub>  $p(1\times 1)$  and (1102)-LaO  $p(1\times 1)$ , whose surface configurations are shown in Figure 3(b), Figure 3(c) and Figure 3(d), respectively. Compared to cubic phase, the O<sub>2</sub> terminated surface is stable under appropriate chemical potential regions, in addition to the LaO<sub>3</sub>- and LaO- terminated surfaces that were predicted to exist in cubic phase.<sup>17</sup> This may be related to the J-T distortion between hexagonal and cubic phase which affects the oxygen binding on the surface. The (1102)-LaO  $p(1\times 1)$  (Figure 3(d)) covers the most part of the diagram. This may be attributed to the fact that (1102)-LaO  $p(1\times 1)$  surface does not require cleaving stable CoO<sub>6</sub> octahedrons, which keeps the system in a relative stable structure. As shown in Figure 3(d), both La and O atoms in the surface are located on their crystalline lattice positions except small out-of-surface displacements. The other two terminations, (1104)-O<sub>2</sub>  $c(2\times 2)$  and (0001)-LaO<sub>3</sub>  $p(1\times 1)$  would become the most stable surfaces only in O- and Co-rich environments, respectively. Under realistic experimental conditions, the range of accessible oxygen chemical potential would generally be within the range of -0.2 to -0.6 eV.<sup>58</sup> We therefore choose  $\Delta\mu_{\text{O}} = -0.40$  eV (marked as the dotted line in Figure 3a) as a representative case and plot the grand potential  $\Omega_s$  of different facets with Co increasing from -8.35 to 0 eV in

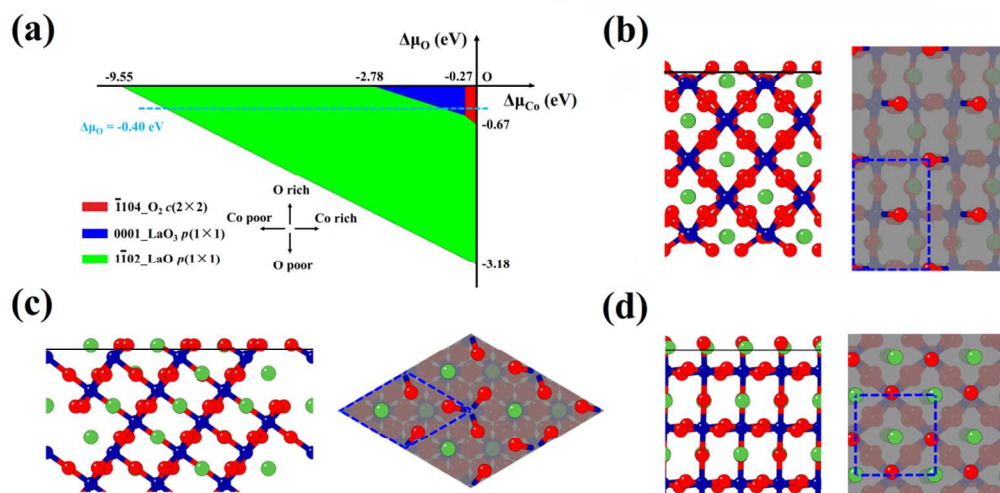


**Fig.3** (a) The stability graph of low-index surfaces of the hexagonal LaCoO<sub>3</sub>. The actual most stable termination is represented as a function of the excess O and Co chemical potentials  $\Delta\mu_{\text{O}}$  ( $\Delta\mu_{\text{O}} = \mu_{\text{O}} - \mu_{\text{O}}^0$ , vertical) and  $\Delta\mu_{\text{Co}}$  ( $\Delta\mu_{\text{Co}} = \mu_{\text{Co}} - \mu_{\text{Co}}^0$ , horizontal). The side and top view of (b) (1104)-O<sub>2</sub>  $c(2\times 2)$ , (c) (0001)-LaO<sub>3</sub>  $p(1\times 1)$  and (d) (1102)-LaO  $p(1\times 1)$  surfaces in (a).

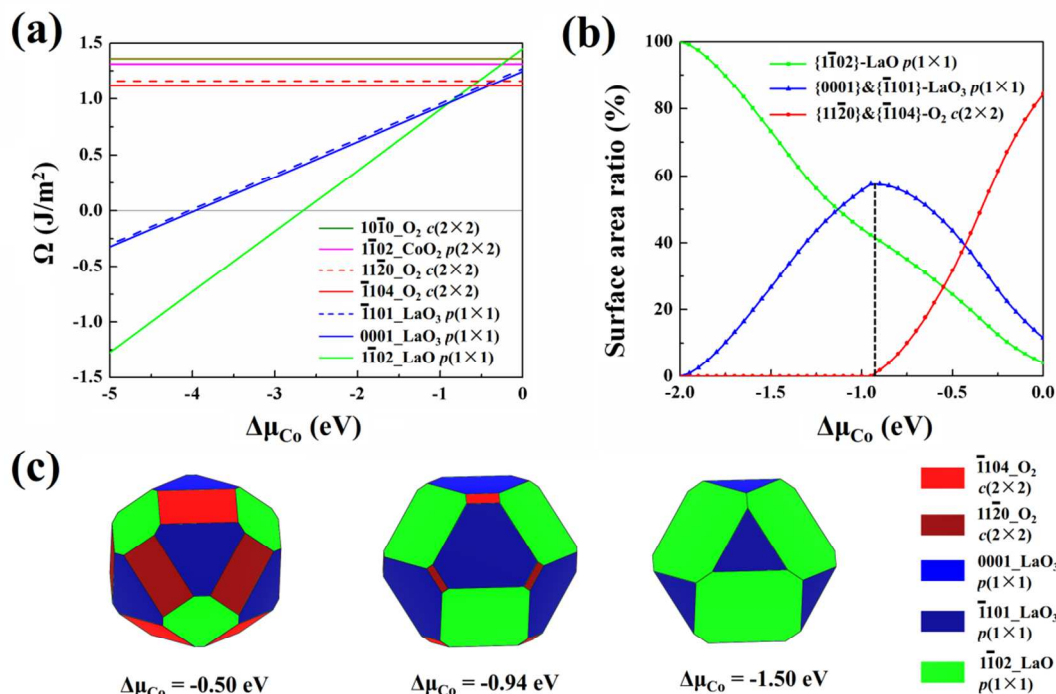


**Fig.4** (a) Stability diagram of different terminations of LaCoO<sub>3</sub> with  $\Delta\mu_{\text{O}} = -0.40$  eV. (b) The relationship between the area of exposed surfaces of NPs and  $\Delta\mu_{\text{Co}}$ . (c) The nanoparticles by Wulff-construction with different  $\Delta\mu_{\text{Co}}$ .

5 Figure 4(a). Shifting to other oxygen chemical potentials within the accessible range would only yield minor numerical corrections without changing the overall picture on reaction mechanism. When  $\Delta\mu_{\text{Co}}$  is very negative,  $\{1\bar{1}02\}\text{-LaO}$  p(1×1) is most stable. By increasing  $\Delta\mu_{\text{Co}}$  along the dotted line, the concentration of La atoms decreases in the environment. Consequently, surfaces with lower La coverage ( $\theta_{\text{La}}$ ) become more stable. When  $\Delta\mu_{\text{Co}} > -0.88$  eV, the  $\{0001\}\text{-LaO}_3$  p(1×1) with  $\theta_{\text{La}} = 0.25$  becomes the most stable facet. Further, when  $\Delta\mu_{\text{Co}}$  increases to  $-0.27$  eV, corresponding to the extremely La-poor condition, the ground stable facet turns to the  $\{1\bar{1}04\}\text{-O}_2$  c(2×2) termination on which  $\theta_{\text{La}} = 0$ . Interestingly, in the whole accessible region, none of the most stable surface contains directly exposed Co atoms. One possible explanation is the dangling  $3d-e_g$  orbitals of Co atoms are energetically unfavorable when exposed on surfaces.

### 3.3. Nano-particles and exposed facets

Based on the calculated  $\Omega$ , we have constructed LaCoO<sub>3</sub> nanoparticles (NPs) at different  $\Delta\mu_{\text{Co}}$  with  $\Delta\mu_{\text{O}} \equiv -0.40$  eV using the Wulff-construction method. It should be noted that Wulff-constructions only applies to bulk particles in a strict sense. However, given the relatively large diameter of oxide nanoparticles, the Wulff-construction should serve as a good first-order approximation.<sup>59</sup> We present quantitatively in Figure 4(b) the area of exposed surfaces of NPs as a function of  $\Delta\mu_{\text{Co}}$ . The area of  $\{1\bar{1}04\}\text{-O}_2$  and  $\{1\bar{1}\bar{2}0\}\text{-O}_2$  is sensitive to  $\Delta\mu_{\text{Co}}$ : they cover 84% of the total area when  $\Delta\mu_{\text{Co}} = 0$  eV, but completely disappear when  $\Delta\mu_{\text{Co}}$  decreases to  $-0.96$  eV. On the other hand,

$\{1\bar{1}01\}\text{-LaO}_3$  facets become dominant with  $-1.12$  eV  $< \Delta\mu_{\text{Co}} < -0.43$  eV. When  $\Delta\mu_{\text{Co}}$  is  $-0.94$  eV, its coverage reaches the maximum (58%). When  $\Delta\mu_{\text{Co}}$  is lower than  $-2.00$  eV,  $\{1\bar{1}02\}\text{-LaO}$  is the only exposed surface. Due to the complicated dependence of exposed surfaces on environments, it is necessary to examine the catalytic activity of each surface in order to predict the best working conditions of LaCoO<sub>3</sub> NPs.

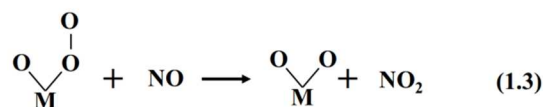
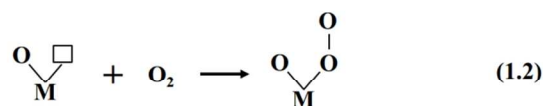
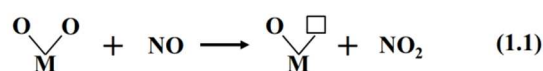
We present three representative shapes of generated NPs in three specific  $\Delta\mu_{\text{Co}}$  ranging from Co poor to Co rich conditions in Figure 4(c). When  $\Delta\mu_{\text{Co}} = -0.50$  eV, the profile of a NP has twenty-six facets, which are 6  $\{1\bar{1}04\}\text{-O}_2$ , 6  $\{1\bar{1}\bar{2}0\}\text{-O}_2$ , 2  $\{0001\}\text{-LaO}_3$ , 6  $\{1\bar{1}01\}\text{-LaO}_3$  and 6  $\{1\bar{1}02\}\text{-LaO}$  facets, respectively. As shown in Figure 4(a),  $\Omega$  of  $\{1\bar{1}01\}\text{-LaO}_3$  p(1×1) is parallel to and only slightly higher than that of  $\{0001\}\text{-LaO}_3$  p(1×1), because their structure are similar except for the slight displacement of oxygen atoms. Thus although only three facets appear in the stability diagram of Figure 3(c),  $\{1\bar{1}01\}\text{-LaO}_3$  and  $\{1\bar{1}\bar{2}0\}\text{-O}_2$ , may also expose on the surface and participate in the catalytic reaction.  $\{1\bar{1}\bar{2}0\}\text{-O}_2$  and  $\{1\bar{1}04\}\text{-O}_2$  have the same tendency. By changing the value of  $\Delta\mu_{\text{Co}}$ , the relative area of the exposed terminations will vary accordingly. The area of  $\{1\bar{1}04\}\text{-O}_2$  and  $\{1\bar{1}\bar{2}0\}\text{-O}_2$  decreases considerably when  $\Delta\mu_{\text{Co}}$  decreases from  $-0.50$  eV to  $-0.94$  eV. Moreover, when  $\Delta\mu_{\text{Co}} < -1.50$  eV,  $\Omega$  of  $\{1\bar{1}02\}\text{-LaO}$  termination is much lower than others. The NP therefore tends to exhibit a cubic shape wrapped by 6  $\{1\bar{1}02\}\text{-LaO}$  facets.

### 3.4. NO oxidation kinetics

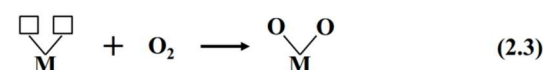
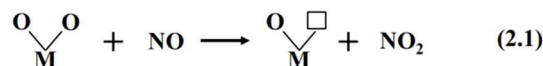
NO oxidation processes on the LaCoO<sub>3</sub> facets is primarily via the Mars-van Krevelen (M-vK) mechanism<sup>60</sup> which is also the

dominant mechanism in many other oxidation processes on metal oxides surfaces.<sup>61,62</sup> Moreover, the results of temperature programmed desorption and isotopic exchange (TPIE) experiments by Choi et al. also indicate that surface species and oxygen exchange processes correlate with NO oxidation activity, which is also consistent with the M-vK mechanism.<sup>22</sup> For NO oxidation, the M-vK mechanism consists of two typical steps, 1) a NO molecule reacts with one lattice O atom and forms NO<sub>2</sub>, 2) an O<sub>2</sub> molecule occupies the created oxygen vacancy from the previous step, creating an active adsorbed O\* species and react with another NO molecule. This scenario can be regarded as mono-vacancy (Mv) M-vK mechanism, as shown in scheme 1. We also have considered the di-vacancy (Dv) M-vK mechanism in which two NO molecules react with two O atoms from lattice sites sequentially, and two vacancies are subsequently filled via the dissociation of O<sub>2</sub>, completing a full catalytic cycle, as shown in scheme 2.

We first calculated  $E_{Ov}$  of the possible exposed surfaces and listed the results in Table 2. The (1̄102)-LaO  $p(1\times 1)$  surface has the highest  $E_{Ov}$  (4.18 eV), which suggests that this surface is not active since O atoms binds too strong to lattice sites and are difficult to escape. The other two re-constructed surfaces, (1̄104)-O<sub>2</sub>  $c(2\times 2)$  and (112̄0)-O<sub>2</sub>  $c(2\times 2)$ , exhibit somewhat lower but still considerably high  $E_{Ov}$  at 2.29 eV and 2.74 eV, respectively. Since the reconstructed surfaces intrinsically have considerable amount of isolated O vacancies (Figure 3b) that may play a role in the oxidation process, these two surfaces are included in our following discussions. On the other hand, the  $E_{Ov}$  of (0001)-LaO<sub>3</sub>  $p(1\times 1)$  and (1̄101)-LaO<sub>3</sub>  $p(1\times 1)$  surfaces are close to zero, indicating the high activity of O atoms and the relative easiness of oxygen vacancy formation on these facets. Thus in addition to reaction routes on an ideal surface, NO oxidation on these facets with oxygen vacancies present was also taken into account.



**Scheme 1.** The sequence of elementary steps for NO oxidation on oxide surface based on Mv M-vK mechanism.



**Scheme 2.** The sequence of elementary steps for NO oxidation on oxide surface based on Dv M-vK mechanism.

**Table 2.** The oxygen vacancy formation energy ( $E_{Ov}$ ) of possible exposed surfaces by Wulff-construction.

Surfaces	(1̄102)- LaO $p(1\times 1)$	(0001)- LaO <sub>3</sub> $p(1\times 1)$	(1̄101)- LaO <sub>3</sub> $p(1\times 1)$	(1̄104)- O <sub>2</sub> $c(2\times 2)$	(112̄0)- O <sub>2</sub> $p(2\times 2)$
$E_{Ov}$ (eV)	4.38	0.09	0.19	2.29	2.74

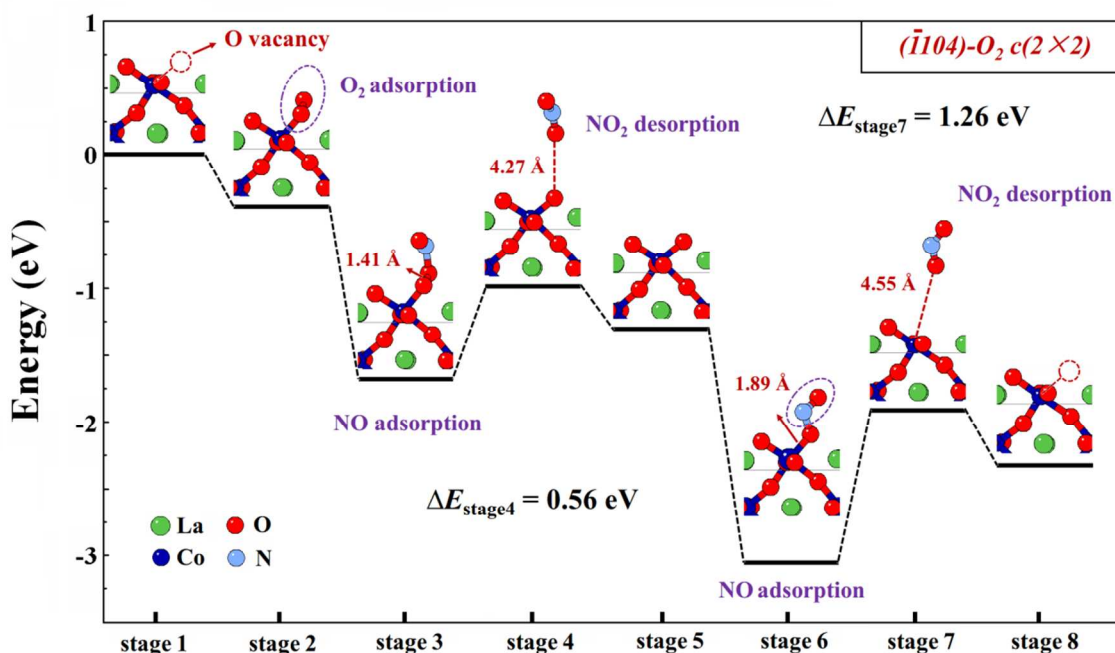


**Fig.5** Energetic scenario of NO oxidation on (1̄104)-O<sub>2</sub>  $c(2\times 2)$  termination, which starts with O<sub>2</sub> molecule occupying the O vacancy on the surface and the total reaction can be summarized as  $2\text{NO} + \text{O}_2 \rightarrow 2\text{NO}_2$ , exothermally.

MEP of NO oxidation on  $(\bar{1}104)\text{-O}_2$   $c(2\times 2)$  re-constructed surface is first discussed and presented in Figure 5, in which stage means a stable state of reactant or product along the reaction path. Due to the high energy cost of removing the second lattice oxygen with  $E_{Ov}$  larger than 2 eV, the vacancy pairing is a rare event and Mv M-vK mechanism is generally the preferred reaction route on the re-constructed surface.<sup>33</sup> According to the Mv M-vK mechanism in scheme 1, the reaction will initiate as (1.2) that an  $\text{O}_2$  molecule will occupy the lattice vacancy and form  $\text{O}_2^*$  (stage 2). Then a NO molecule binds with the protruding O atom and forms an  $\text{NO}_2$  molecule adsorbed to the surface (stage 3 to stage 4). Energy barrier for the detachment of the  $\text{NO}_2$  molecule  $\Delta E_{\text{stage4}}$  is 0.56 eV. The second half of the MEP includes the formation of Co-nitrite ( $-\text{NO}_2$ ) species on the surface resulting from the binding of the second NO molecule and one O atom in lattice sites (stage 6 to stage 7). Among all the reaction path, the  $\text{NO}_2$  desorption is the rate-determining step (RDS) since the corresponding barrier  $\Delta E_{\text{stage7}}$  (1.26 eV) is the highest along the MEP. The whole reaction can be summarized as  $2\text{NO} + \text{O}_2 \rightarrow 2\text{NO}_2$  with 2.31 eV exothermically. In addition, we have calculated MEP of NO oxidation on  $(11\bar{2}0)\text{-O}_2$   $c(2\times 2)$  surface and the results are presented in Figure S7. We notice the RDS is also the desorption of the  $\text{NO}_2$  molecule with an energy barrier of 1.18 eV, similar to the case of  $(\bar{1}104)\text{-O}_2$   $c(2\times 2)$  surface. It suggests the slight structural variation among different surface orientations within the same group will not affect the catalytic process.

For the  $(0001)\text{-LaO}_3$   $p(1\times 1)$  facets, since the oxygen vacancy formation is small, it is expected that ideal facets and defective facets with oxygen vacancies are likely to co-exist under realistic experimental conditions. Consequently, we have studied MEP of NO oxidation in both cases. The MEP on an ideal  $(0001)\text{-LaO}_3$  surface also follow the Mv M-vK mechanism (Scheme 1) as shown in Figure 6, in which the transition states are labelled as TS. The oxidation reaction initiates with NO (g) adsorbing onto the O site to form Co-nitrite ( $-\text{NO}_2$ ). The adsorbed NO then binds with one O atom from a lattice site and desorbs from the

surface as a  $\text{NO}_2$  molecule. Interestingly, we find that the desorption process are divided into two steps due to the attraction of neighboring La atoms to the  $\text{NO}_2$  molecule, which is consistent with previous experimental results.<sup>63</sup> Firstly, the  $\text{NO}_2$  molecule overcomes an energy barrier of 0.78 eV to desorb from the surface with an oxygen vacancy left behind (stage 2 to stage 3). However, the desorbed  $\text{NO}_2$  molecule is still trapped by a La atom (stage 3). In the second step, the  $\text{NO}_2$  molecule escapes from the La site with an additional barrier of 0.47 eV. This leaves one oxygen vacancy on the surface, and the following step involves a perpendicular adsorption of  $\text{O}_2$  molecule onto the vacancy site. In subsequent steps, the second NO molecule binds to the protruding O atom and form an adsorbed  $\text{NO}_2$  molecule (stage 6 to stage 7) with a desorption barrier of  $\Delta E_{\text{TS2}} = 0.80$  eV, which is the highest energy barrier along the whole reaction path.

For NO oxidation on  $(0001)\text{-LaO}_3$  with oxygen vacancies, since reaction with NO molecules would create an additional oxygen vacancy, the reaction proceeds via the Dv M-vK mechanism. Figure 7 shows the NO oxidation path on  $(0001)\text{-LaO}_3$   $p(1\times 1)$  surface starting with an oxygen vacancy. As shown in Figure 7, the NO oxidation path initiates as (2.2) in Scheme 2 that the vacancy is occupied by an NO molecule. The adsorbed NO would bind to an oxygen nearby the vacancy and form  $\text{NO}_2$ . Similar to the case in Figure 6, the  $\text{NO}_2$  molecule will be trapped by two La atoms and the desorption process is endothermic by 1.18 eV (stage 3 to stage 4). After the desorption of  $\text{NO}_2$ , a di-vacancy is created on the  $(0001)\text{-LaO}_3$   $p(1\times 1)$  surface. Then, the di-vacancy is occupied by  $\text{O}_2$  (stage 5) and the O atoms bind with Co atom to form a stable structure. The dissociation of the  $\text{O}_2$  molecule to fill the di-vacancy shows an activation barrier of 1.54 eV. In the following steps, NO will bind to the ideal surface and reacts with the lattice oxygen with an energy barrier of 0.78 eV as shown in Figure 6. This recovers the  $(0001)\text{-LaO}_3$   $p(1\times 1)$  surface with an oxygen vacancy and completes the NO oxidation cycle. Through the discussion of Figure 7, the RDS step on  $(0001)\text{-LaO}_3$   $p(1\times 1)$  surface based on Dv M-vK mechanism is the oxygen dissociation step and is less favorable than the Mv M-vK mechanism.

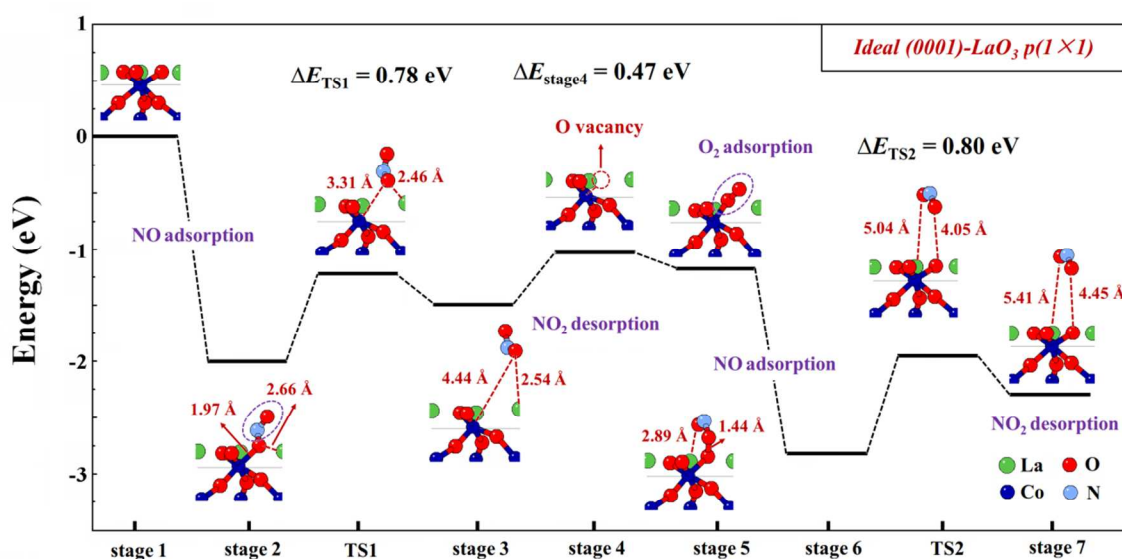


Fig.6 Energetic scenario of NO oxidation on ideal  $(0001)\text{-LaO}_3$   $p(1\times 1)$  surface based on mono-vacancy M-vK mechanism.

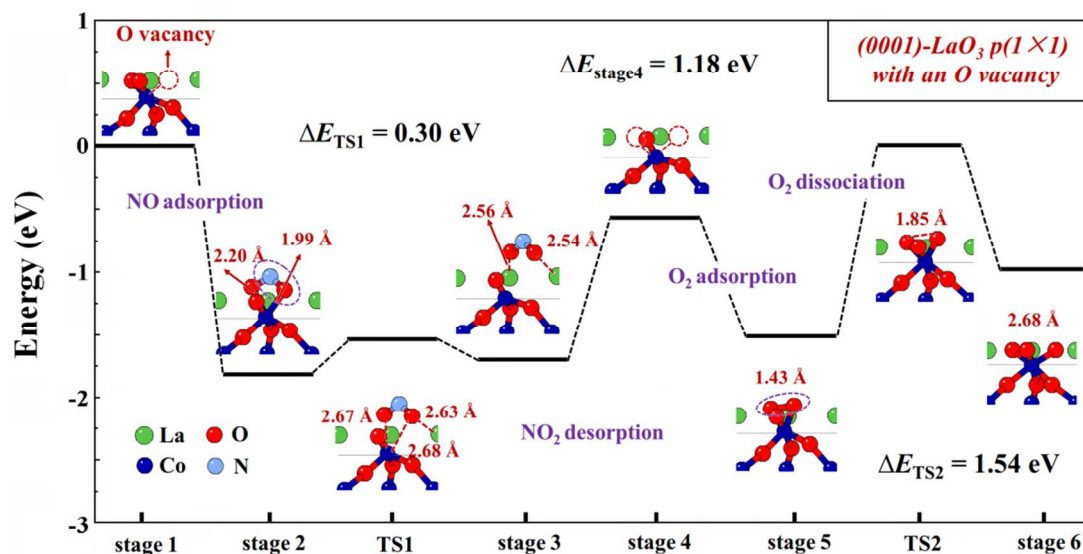


Fig.7 Energetic scenario of NO oxidation on (0001)-LaO<sub>3</sub> p(1×1) surface with an oxygen vacancy based on di-vacancy M-vK mechanism

Based on the above discussions, we conclude that LaO<sub>3</sub> terminated surface has the most promising catalytic activity. RDS are NO<sub>2</sub> desorption and O<sub>2</sub> dissociation for Mv and Dv M-vK mechanism on (0001)-LaO<sub>3</sub>, respectively. However, the Mv M-vK mechanism with lower RDS barrier (0.80 eV) is preferable than Dv M-vK mechanism. The best strategy to improve the catalytic performance of LaCoO<sub>3</sub> NPs is to maximize the area of LaO<sub>3</sub> terminated surfaces, which can be achieved by tuning the surfactants and controlling cobalt chemical potentials during the synthesis procedure.

#### 4. Conclusions

We have systematically studied the stability of differently reconstructed LaCoO<sub>3</sub> surfaces. From the stability point of view, (1104)-O<sub>2</sub> c(2×2), (0001)-LaO<sub>3</sub> p(1×1) and (1102)-LaO p(1×1) facets are thermodynamically most stable. NO oxidation mechanisms on active surfaces have been comprehensively investigated and the (0001)-LaO<sub>3</sub> facet is found to be most active towards NO oxidation. The RDS steps for the Mv- and Dv- M-vK mechanism are NO<sub>2</sub> desorption and O<sub>2</sub> dissociation, respectively. Our results give insight into the reaction mechanism of NO oxidation on hexagonal phase LaCoO<sub>3</sub> and could help further optimization of the perovskite catalyst.

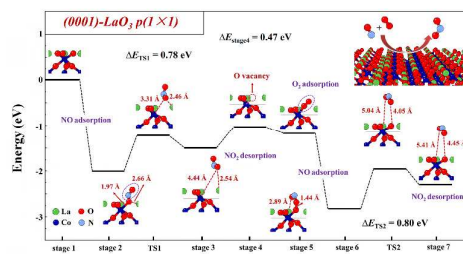
#### Acknowledgments

This work is supported National Basic Research Program of China (2013CB934800 and 2011CB606401) and National Natural Science Foundation of China (Grant 51302094 and 51101064). The authors acknowledge the Thousand Young Talents Plan and New Century Excellent Talents in University (NCET). The calculations are done at the Texas Advanced Computing Center (TACC) at The University of Texas at Austin (<http://www.tacc.utexas.edu>).

#### Notes and references

- <sup>a</sup> State Key Laboratory of Digital Manufacturing Equipment and Technology and School of Mechanical Science and Engineering, Huazhong University of Science and Technology, Wuhan 430074, Hubei, People's Republic of China
- <sup>b</sup> State Key Laboratory of Material Processing and Die and Mould Technology and School of Materials Science and Engineering, Huazhong University of Science and Technology, Wuhan 430074, Hubei, People's Republic of China
- <sup>c</sup> Department of Materials Science and Engineering, The University of Texas at Dallas, Richardson, Texas 75080, USA
- † Electronic Supplementary Information (ESI) available: [Description of the detailed structural information of hexagonal LaCoO<sub>3</sub>]. See DOI:10.1039/b000000x/
- \* Corresponding author e-mail address: [bshah@mail.hust.edu.cn](mailto:bshah@mail.hust.edu.cn) (Bin Shan); [rongchen@mail.hust.edu.cn](mailto:rongchen@mail.hust.edu.cn) (Rong Chen).
- C. H. Bartholomew and R. J. Farrauto, *Fundamentals of Industrial Catalytic Process*, Wiley, Hoboken, N.J., 2006.
  - M. Tas, R. van Hardeveld and E. M. van Veldhuizen, *Plasma Chem. Plasma Proc.*, 1997, **17**, 371-391.
  - B. Hammer, Y. Morikawa and J. K. Nørskov, *Phys. Rev. Lett.*, 1996, **76**, 2141-2144.
  - M. H. Tsai and K. C. Hass, *Phys. Rev. B*, 1995, **51**, 14616-14625.
  - X. W. Xie, Y. Li, Z. Q. Liu, M. Haruta and W. J. Shen, *Nature*, 2009, **458**, 746-749.
  - L. F. Liotta, H. J. Wu, G. Pantaleo and A. M. Venezia, *Catal. Sci. Technol.*, 2013, **3**, 3085-3102.
  - S. Krishnamoorthy, J. A. Rivas and M. D. Amiridis, *J. Catal.*, 2000, **193**, 264-272.
  - J. Wang, Y. G. Su, X. Q. Wang, J. H. Chen, Z. Zhao and M. Q. Shen, *Catal. Commun.*, 2012, **25**, 106-109.
  - X. J. Yao, F. Gao, Q. Yu, L. Qi, C. J. Tang, L. Dong and Y. Chen, *Catal. Sci. Technol.*, 2013, **3**, 1355.
  - F. Can, S. Berland, S. Royer, X. Courtois and D. Duprez, *ACS Catal.*, 2013, **3**, 1120-1132.
  - H. Li, X. L. Tang, H. H. Yi and L. L. Yu, *J. Rare Earth.*, 2010, **28**, 64-68.

- 12 W. C. Wang, G. McCool, N. Kapur, G. Yuan, B. Shan, M. Nguyen, U. M. Graham, B. H. Davis, G. Jacobs, K. Cho and X. H. Hao, *Science*, 2012, **337**, 832-835.
- 13 Y. X. Wen, C. B. Zhang, H. He, Y. B. Yu and Y. Teraoka, *Catal. Today*, 2007, **126**, 400-405.
- 14 C. Zhou, X. Liu, C. Z. Wu, Y. W. Wen, Y. J. Xue, R. Chen, Z. L. Zhang, B. Shan, H. F. Yin and W. G. Wang, *Phys. Chem. Chem. Phys.*, 2014, **16**, 5106-5112.
- 15 C. H. Kim, G. S. Qi, K. Dahlberg and W. Li, *Science*, 2010, **327**, 1624-1627.
- 16 S. Khan, R. J. Oldman, F. Corà, C. Catlow, S. French and S. A. Axon, *Phys. Chem. Chem. Phys.*, 2006, **8**, 5207-5222.
- 17 Z. Z. Chen, C. H. Kim, L. Thompson and W. F. Schneider, *Surf. Sci.*, 2014, **619**, 71-76.
- 18 P. Ravindran, P. A. Korzhavyi, H. Fjellvåg and A. Kjekshus, *Phys. Rev. B*, 1999, **60**, 16423-16434.
- 19 S. Mukhopadhyay, M. W. Finnis and N. M. Harrison, *Phys. Rev. B*, 2013, **87**, 125132.
- 20 M. Risch, A. Grimaud, K. J. May, K. A. Stoerzinger, T. J. Chen, A. N. Mansour and Y. Shao-Horn, *J. Phys. Chem. C*, 2013, **117**, 8628-8635.
- 21 S. M. Zhou, L. F. He, S. Y. Zhao, Y. Q. Guo, J. Y. Zhao and L. Shi, *J. Phys. Chem. C*, 2009, **113**, 13522-13526.
- 22 S. O. Choi, M. Penninger, C. H. Kim, W. F. Schneider and L. T. Thompson, *ACS Catal.*, 2013, **3**, 2719-2728.
- 23 Y. L. Lee, J. Kleis, J. Rossmeisl and D. Morgan, *Phys. Rev. B*, 2009, **80**, 224101.
- 24 A. Kushima, S. Yip and B. Yildiz, *Phys. Rev. B*, 2010, **82**, 115435.
- 25 P. Hohenberg and W. Kohn, *Phys. Rev.*, 1964, **136**, B864-B871.
- 26 W. Kohn and L. J. Sham, *Phys. Rev.*, 1965, **140**, A1133-A1138.
- 27 G. Kresse and J. Hafner, *Phys. Rev. B*, 1993, **47**, 558-561.
- 28 G. Kresse and J. Hafner, *Phys. Rev. B*, 1994, **49**, 14251-14269.
- 29 G. Kresse and J. Hafner, *Comput. Mater. Sci.*, 1996, **6**, 15-50.
- 30 J. P. Perdew, K. Burke and M. Ernzerhof, *Phys. Rev. Lett.*, 1996, **77**, 3865-3868.
- 31 G. Kresse and D. Joubert, *Phys. Rev. B*, 1999, **59**, 1758-1775.
- 32 H. Y. Kim and G. Henkelman, *J. Phys. Chem. Lett.*, 2012, **3**, 2194-2199.
- 33 H. Y. Kim and G. Henkelman, *J. Phys. Chem. Lett.*, 2013, **4**, 216-221.
- 34 V. I. Anisimov, J. Zaanen and O. K. Andersen, *Phys. Rev. B*, 1991, **44**, 943.
- 35 A. Rohrbach, J. Hafner and G. Kresse, *Phys. Rev. B*, 2004, **69**, 075413.
- 36 A. Rohrbach and J. Hafner, *Phys. Rev. B*, 2005, **71**, 045405.
- 37 C. L. Ma and J. Cang, *Solid State Commun.*, 2010, **150**, 1983-1986.
- 38 F. Aryasetiawan and O. Gunnarsson, *Rep. Prog. Phys.*, 1998, **61**, 237.
- 39 G. Onida, L. Reining and A. Rubio, *Rev. Mod. Phys.*, 2002, **74**, 601.
- 40 J. Heyd, G. E. Scuseria and M. Ernzerhof, *J. Chem. Phys.*, 2003, **118**, 8207.
- 41 J. Heyd, G. E. Scuseria and M. Ernzerhof, *J. Chem. Phys.*, 2006, **124**, 19906.
- 42 H. J. Monkhorst and J. D. Pack, *Phys. Rev. B*, 1976, **13**, 5188.
- 43 F. Bottin, F. Finocchi and C. Noguera, *Phys. Rev. B*, 2003, **68**, 035418.
- 44 G. H. Chen, Z. F. Hou and X. G. Gong, *Comp. Mater. Sci.*, 2008, **44**, 46-52.
- 45 C. Herring, *Phys. Rev.*, 1951, **82**, 87.
- 46 K. Momma and F. Izumi, *J. Appl. Cryst.*, 2011, **44**, 1272-1276.
- 47 G. Henkelman and H. Jónsson, *J. Chem. Phys.*, 2000, **113**, 9978-9985.
- 48 P. G. Radaelli and S. W. Cheong, *Phys. Rev. B*, 2002, **66**, 094408.
- 49 A. Chainani, M. Mathew and D. D. Sarma, *Phys. Rev. B*, 1992, **46**, 9976-9983.
- 50 I. A. Nekrasov, S. V. Streltsov, M. A. Korotin and V. I. Anisimov, *Phys. Rev. B*, 2003, **68**, 235113.
- 51 J. Kuneš and V. Krápek, *Phys. Rev. Lett.*, 2011, **106**, 256401.
- 52 S. K. Pandey, A. Kumar, S. Patil, V. R. R. Medicherla, R. S. Singh, K. Maiti, D. Prabhakaran, A. T. Boothroyd and A. V. Pimpale, *Phys. Rev. B*, 2008, **77**, 045123.
- 53 H. Y. Wang and W. F. Schneider, *Catal. Today*, 2011, **165**, 49-55.
- 54 H. Y. Wang, W. F. Schneider and D. Schmidt, *J. Phys. Chem. C*, 2009, **113**, 15266-15273.
- 55 J. Zhou, G. Chen, K. Wu and Y. H. Cheng, *J. Phys. Chem. C*, 2013, **117**, 12991-12999.
- 56 C. Noguera, *J. Phys.: Condens. Matter*, 2000, **12**, R367.
- 57 F. Bechstedt, *Principles of Surface Physics*, Springer-Verlag, New York, 2003.
- 58 K. Reuter and M. Scheffler, *Appl. Phys. A*, 2004, **78**, 793.
- 59 S. Piccinin, S. Zafeirotas, C. Stampfl, T. W. Hansen, M. Hävecker, D. Teschner, V. I. Bukhtiyarov, F. Girgsdies, A. Knop-Gericke, R. Schlögl and M. Scheffler, *Phys. Rev. Lett.*, 2010, **104**, 035503.
- 60 P. Mars and D. W. Van Krevelen, *Chem. Eng. Sci.*, 1954, **3**, 41-59.
- 61 W. Y. Song and E. J. M. Hensen, *Catal. Sci. Technol.*, 2013, **3**, 3020-3029.
- 62 H. Y. Kim, H. M. Lee and G. Henkelman, *J. Am. Chem. Soc.*, 2012, **134**, 1560-1570.
- 63 Z. Say, M. Dogac, E. I. Vovk, Y. E. Kalay, C. H. Kim, W. Li and E. Ozensoy, *Appl. Catal. B: Environ.*, 2014, **154**, 51-61.



The surface stability of hexagonal-phase LaCoO<sub>3</sub> has been studied and LaO<sub>3</sub>-terminated surface is catalytically most active towards NO oxidation.